SOFT ROBOTS

An untethered isoperimetric soft robot

Nathan S. Usevitch[1]*†, Zachary M. Hammond[1]*†, Mac Schwager[2], Allison M. Okamura[1], Elliot W. Hawkes[3]‡, Sean Follmer[1]‡

For robots to be useful for real-world applications, they must be safe around humans, be adaptable to their environment, and operate in an untethered manner. Soft robots could potentially meet these requirements; however, existing soft robotic architectures are limited by their ability to scale to human sizes and operate at these scales without a tether to transmit power or pressurized air from an external source. Here, we report an untethered, inflated robotic truss, composed of thin-walled inflatable tubes, capable of shape change by continuously relocating its joints, while its total edge length remains constant. Specifically, a set of identical roller modules each pinch the tube to create an effective joint that separates two edges, and modules can be connected to form complex structures. Driving a roller module along a tube changes the overall shape, lengthening one edge and shortening another, while the total edge length and hence fluid volume remain constant. This isoperimetric behavior allows the robot to operate without compressing air or requiring a tether. Our concept brings together advantages from three distinct types of robots—soft, collective, and truss-based—while overcoming certain limitations of each. Our robots are robust and safe, like soft robots, but not limited by a tether; are modular, like collective robots, but not limited by complex subunits; and are shape-changing, like truss robots, but not limited by rigid linear actuators. We demonstrate two-dimensional (2D) robots capable of shape change and a human-scale 3D robot capable of punctuated rolling locomotion and manipulation, all constructed with the same modular rollers and operating without a tether.

INTRODUCTION

For robots to work in conjunction with humans and be useful outside of highly engineered environments, they must be human-safe, robust, adaptable to a variety of scenarios, and capable of moving through diverse types of terrain. These attributes require not only adaptable control algorithms and the collection and processing of rich sensory information but also new forms of reconfigurable, adaptable robotic structures, which are potentially soft in nature.

We present a concept for such a robotic structure: a truss of inextensible, inflatable, constant-length tubes that are manipulated by a collective of interconnected roller modules, allowing for shape change and compliance without a pressure source (Fig. 1A). Pressurized tubes serve as structural elements and the edges of the truss. Each joint in the tubing is formed by a robotic roller module that pinches the tube between cylindrical rollers without creating a seal. The roller modules can be connected to neighboring modules to form a node of a complex two-dimensional (2D) or 3D structure. An electric motor and mechanical transmission then drive these rollers like wheels along the tube, causing the pinch point to translate (Fig. 1B). Edge lengths of the robot are changed not by stretching or contracting the edges but by movement of the roller module along the tube—moving the effective joint and simultaneously lengthening one edge while shortening another (Fig. 1C and movie S1). The sum of all the edge lengths remains constant; therefore, we call the robot an isoperimetric system (constant perimeter). A gap between the rollers ensures that as they move, there is negligible pressure difference between the two edges, leading to a system with constant volume that does not require a pressure source. The individual roller modules are simple and capable of moving along the tube in only one degree of freedom, yet the overall collective is capable of complex behavior.

Our robotic concept is built upon a combination of concepts from collective robots, truss robots, and soft robots. This allows us to realize a unique set of traits, because we exploit advantages while bypassing certain disadvantages of each individual type of robot.

As a collective system of robots, our concept is inherently modular with interchangeable, simple (one degree of freedom) subunit roller modules. However, because our subunits are physically interconnected through a compliant network, the collective achieves complex system-level behavior, capable of applying forces in three dimensions on a large scale. This overcomes a limitation of collective robots that combine together to create structures that can change their shape (*1*–*4*)—realizing complex 3D physical interaction while maintaining simplicity at the individual robot level. A related type of collective robotic system uses teams of robots that build passive structures (*5*–*8*). The target structure is often truss-like, built by adding passive elements, and sometimes requires that the robots traverse the structure as they build it. Rather than discretely rearranging passive elements within a structure to change its shape, in our concept, the collective continuously deforms passive bodies to change the locations of where the bodies are attached, resulting in very simple robotic subunits.

As a truss-like robot—which has been proposed for intriguing applications like exploring planets (*9*–*12*), burrowing underground (*13*), shoring up rubble (*14*, *15*), and modular robotic systems (*16*, *17*)—our concept is adaptable and customizable. However, because our robot has a compliant structure and moves without requiring linear actuators, it affords robustness that is lacking in other truss-like robots. Ideally, the linear actuators of a truss robot would be lightweight, be robust, have a high extension ratio, and operate untethered. Although certain new actuators meet some of these requirements (*18*–*21*), achieving all is challenging. This means that when existing actuators

[1]Department of Mechanical Engineering, Stanford University, Stanford, CA, USA. [2]Department of Aeronautics and Astronautics, Stanford University, Stanford, CA, USA. [3]Department of Mechanical Engineering, University of California, Santa Barbara, Santa Barbara, CA, USA.
*These authors contributed equally to this work.
†Corresponding author. Email: usevitch@stanford.edu (N.S.U.); zhammond@stanford.edu (Z.M.H.)
‡These authors contributed equally to this work.

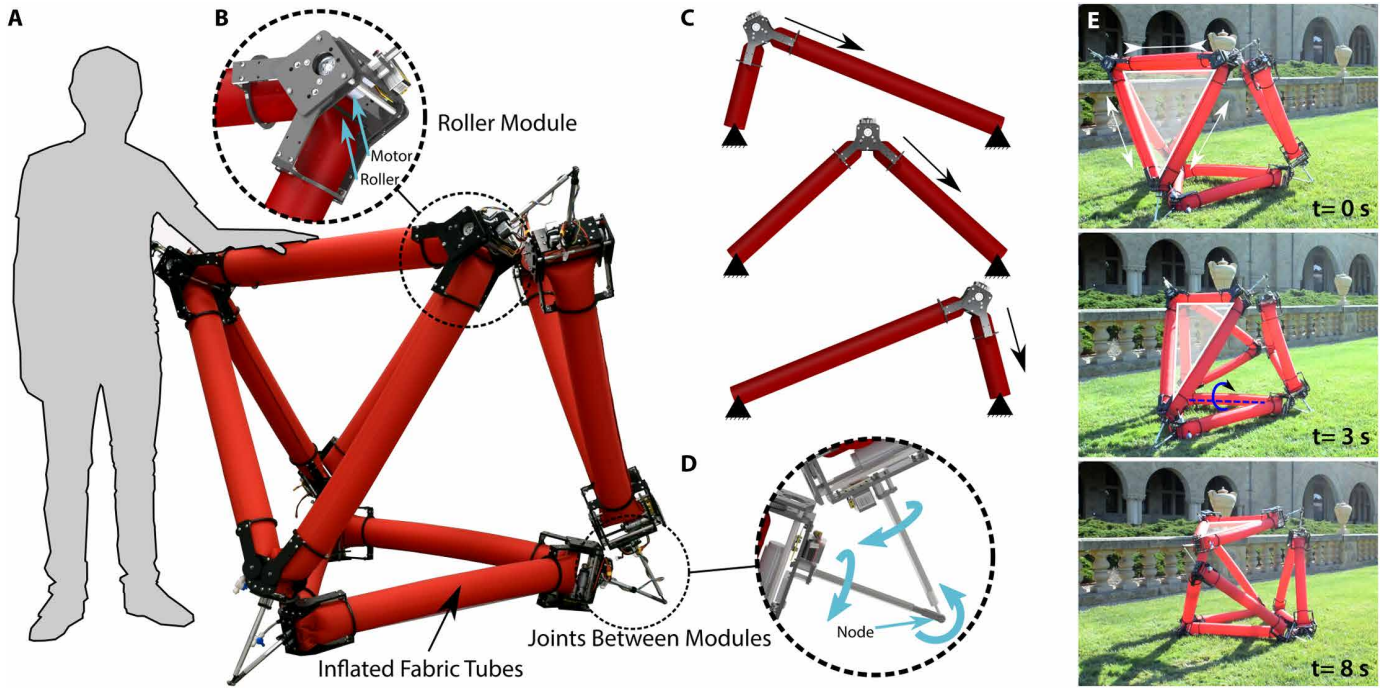

Fig. 1. An overview of the components and operating principle of the robot. (**A**) A large-scale inflated robot that does not require a tether. The robot is composed of a set of identical robotic roller modules that are mounted onto inflated fabric tubes that form the primary structure of the robot. (**B**) The rollers pinch the fabric tube between rollers, creating an effective joint that can be relocated by driving the rollers. (**C**) The roller modules actuate the robot by driving along the tube, simultaneously lengthening one edge while shortening another. The roller modules can connect to one another to construct 2D and 3D truss-like structures capable of shape change and locomotion. (**D**) The roller modules connect to each other at nodes using three-degree-of-freedom universal joints that are composed of a clevis joint that couples two rods, each free to spin about its axis. The arrows indicate how the joints can rotate. (**E**) The robot locomotes untethered outdoors using a punctuated rolling gait. One face of the robot is highlighted to illustrate the rolling motion.

are connected into a truss system, the resulting robot is relatively rigid, slow, heavy, and lacking in robustness to large impacts. Our robot overcomes some of the challenges of conventional truss robots because the structure is composed of lightweight compliant pneumatic beams. Tensegrity robots also overcome the fragility of truss robots, but through a network of compliant cables or compliant beams that create part of their structure (*22*–*28*). Tensegrity robots can undergo large shape changes, especially volume changes for deployment, but the fact that typically only a subset of edges change length, and some edges may only support tensile loads, imposes some constraints on the possible shape change. Our robot is not a tensegrity robot, but it incorporates the compliant characteristics that have made tensegrity robots more robust, to enable tough robots that are highly adaptable.

As a soft robot, our concept is inherently human-safe and has a high tolerance to uncertainty in the environment (*29*–*33*). However, because it is a constant-volume, isoperimetric system (nodes move, but the total length of the pneumatic structure remains the same), it overcomes a fundamental limitation of pneumatic soft robots—the air supply. Previous methods to provide pneumatic power onboard include carrying a microcompressor (*34*, *35*), carrying a pressurized fluid reservoir (*36*), using chemical decomposition (*37*), and using explosive fuels (*38*, *39*). However, each of these is limited: Microcompressors have low flow rates and peak pressures, compressed air in a reservoir has limited overall capacity, and chemical decomposition or burning of a fuel often requires system-level integration and does not easily provide air at useful pressures and rates (*40*). In contrast, other soft systems use a fixed amount of air within a cavity as a structural element and not as an actuator, requiring no pressure source once the cavity is pressurized (*41*–*46*). Some of this work has exhibited direct manipulation of the membrane of an inflated beam to create bending without compressing the air within (*42*, *43*). We built upon this work for our soft, untethered robot, but instead of manipulating a serial robot by deforming the membrane around fixed joints as in (*42*, *43*), we continuously moved the effective joints along the structure, which allowed large, global shape change of a truss-like robot.

Here, we present demonstrations and characterizations of the collective, truss-like, and soft nature of our robots. To highlight the collective and modular nature of the robot, we present three different robots, two 2D robots and one 3D robot, each constructed from identical one-degree-of-freedom roller modules, yet as a collective, capable of complex movement. To demonstrate the truss-like nature of the robot, we show marked shape change of all three of the robots and punctuated rolling locomotion of the 3D robot. To demonstrate and characterize the softness of the robot, we show its robustness to crushing forces, measure its behavior under load, and leverage its compliance to grasp and manipulate objects. Each of these demonstrations is conducted with the robot untethered from a pressure source. Last, we present the models and experiments that inform the mechanical design of the subcomponents of the robots and provide insights into the tradeoffs among our robots, truss robots, and pneumatically actuated robots through theoretical analysis of reachable workspace, efficiency, and speed.

RESULTS

2D collective demonstrating truss-like shape change

We demonstrate the collective and modular nature of the isoperimetric concept by constructing two different 2D robots with the same roller modules (Fig. 2). The first robot is composed of three separate tubes, and the second is composed of a single tube. Robots with multiple tubes are interesting because the modularity is extended to robotic substructures containing multiple roller modules. For example, substructures designed for specific tasks, like grasping or locomotion, could be combined to form a variety of robots. On the other hand, robots with a single tube have fewer constraints on their configuration and larger maximum edge lengths. With both robots, we demonstrate a truss-like shape-changing ability.

For the first robot, each of the three individual tubes (3.4 m long and 0.1 m diameter) was routed through two active roller modules before affixing its ends to a passive module that did not contain a motor, creating a triangle. The triangular substructures were then assembled by connecting pairs of roller modules with revolute joints, showing that complex robots can be assembled from multiple simpler robots. The robot could deploy from a small area of 0.85 m^2 without human intervention when air was added from an external source (Fig. 2A). After the robot was inflated to an operating pressure of

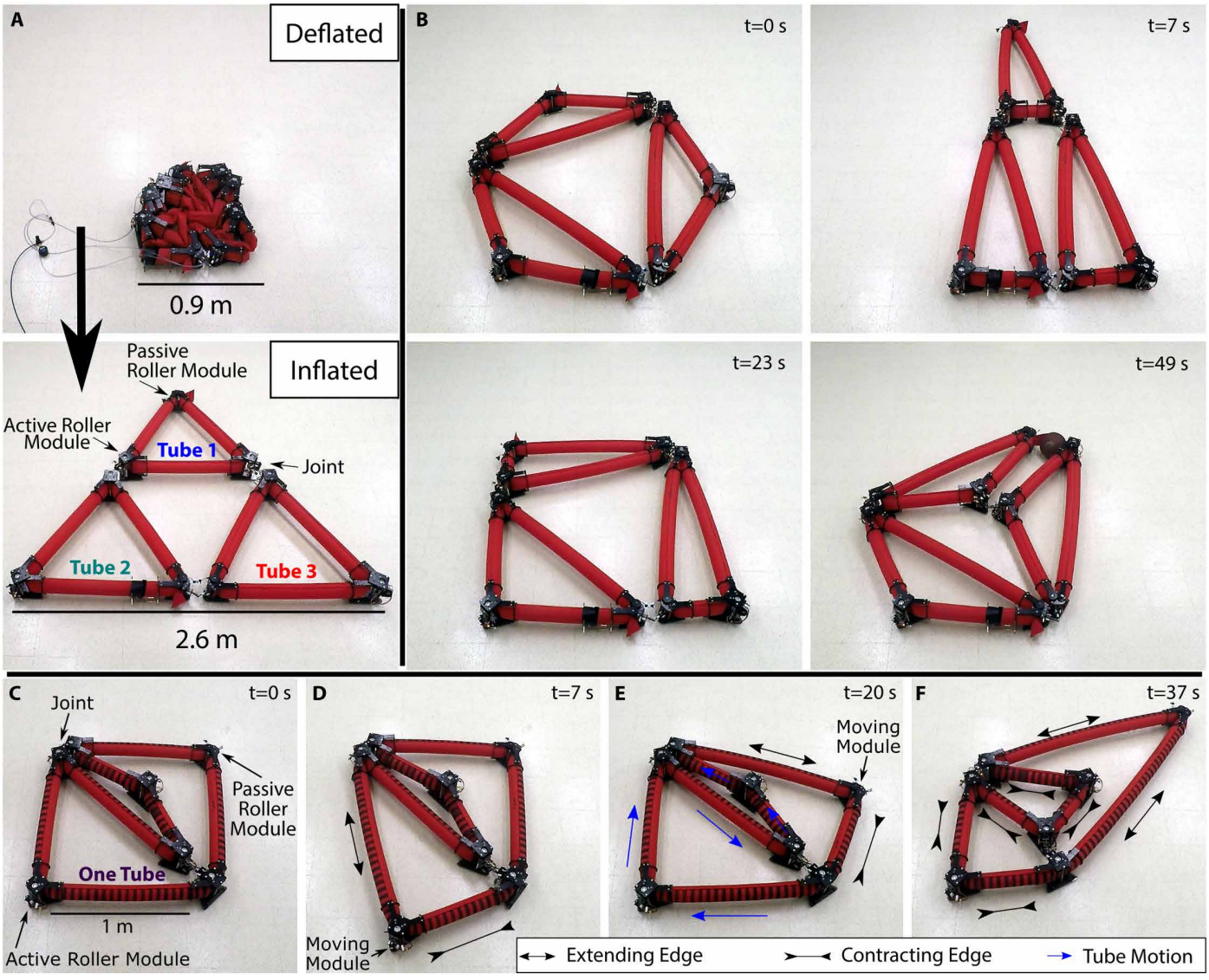

Fig. 2. Demonstrations of two different 2D robots, each a collective of the same roller modules with different tube architectures, showing truss-like shape change. (**A**) A robot, formed from three separate tubes that are routed into triangles and connected together, inflates and springs into shape without intervention. (**B**) This three-tube robot can change to a variety of shapes. Casters under the roller modules allow motion. (**C**) A robot composed of a single inflated tube can markedly lengthen its edges, because each edge can exchange material with any other edge. The single-tube design also means that sometimes roller modules must run to pass material through the network, even if the edge lengths immediately connected to it are not changing length. (**D**) A single active roller module moves, causing one adjacent edge to shorten and the other to lengthen. (**E**) To lengthen and shorten the two edges adjacent to the passive module, all the active roller modules move in coordination. (**F**) The single-tube configuration is capable of much larger edge lengths because all other edges can shorten to accommodate the lengthening of two edges.

40 kPa (and an area of 2.9 m^2), we removed the tether and drove the roller modules to demonstrate a few feasible shapes: a tall skinny triangle, a hexagon, a square, and a "pincer" shape that could grasp an object (Fig. 2B). It took less than 50 s for the robot to transition among all four of these shapes (movie S2). The minimum length of an edge was 28 cm for this prototype and was fixed by the size of the roller module.

For the second robot, we routed a single tube with a length of 6.8 m through eight active roller modules and a single passive module, as shown in Fig. 2C and movie S3. This single-tube architecture enabled certain behaviors that were not possible with the first, three-triangle architecture, where an edge could only lengthen if another edge in the same triangle shortens. In contrast, when a single tube was used for the entire robot, the material could be exchanged between any two edges in the network. To exchange length between edges that are adjacent, one roller module moved along the tube (Fig. 2D). For edges that are not adjacent, all intermediate powered roller modules must roll to transfer the tube material, even if the edges adjacent to the intermediate roller modules do not change length (Fig. 2E). Because any edge in the robot can contribute length to any other edge, much larger maximum edge lengths could be reached with the single-tube architecture (Fig. 2F), illustrating that the maximum length of an edge depends on the robot architecture.

3D octahedron robot: Truss-like shape change and locomotion

We used the same roller modules from the 2D robots to create a 3D octahedron, formed by connecting four individual triangles, each with a tube length of 3.4 m. As before, a triangle has two active and one passive modules. We demonstrated truss-like 3D shape-changing and locomotion.

The first demonstration of the 3D robot explored its volume change during deployment (Fig. 3A). The structure could compact to a volume of 0.173 m^3 when deflated (fitting within a 64 cm–by–71 cm–by–38 cm rectangular prism) and then deploy to an octahedron with a volume of 2.29 m^3, increasing by a factor of 13. Next, after untethering the robot, we showed that it is capable of markedly changing its shape, including changing its height by a factor of 2 and moving to an asymmetric configuration where one node extends upward (Fig. 3B and movie S4). Movie S5 shows a simulated robot moving according to our kinematic model (see Materials and Methods) side by side with the real robot moving. Although not a perfect agreement, the character of the robot motion is captured by the simulation. Small errors developed because of imperfections in our current fabrication methods, leading to variations in tube diameter and length. Last, we demonstrated locomotion. The robot could locomote with a punctuated rolling gait at a speed of 2.14 body lengths/minute, or 3.6 m/min (Fig. 3C and movie S6). In the current implementation, each roller module had a battery life of about 23 min under continuous roller movement (see Supplementary Text and fig. S1 for further information).

3D octahedron robot: Compliant behavior and manipulation

The inflated fabric tubes are compliant, a hallmark of soft robots and a property that affords robustness to the structure. To demonstrate this robustness (Fig. 4A and movie S7), we loaded the robot with a wooden pallet before increasing the load until structural failure (Fig. 4A). When the load was removed and external forces were applied to restore the structure to its initial shape, it was again able to support the initial load, undamaged. To quantify the response of the robot under load, we measured force while displacing the top roller module of a single triangle in three different configurations using the experimental setup described in Supplementary Text and fig. S5. The results are shown in Fig. 4B. When an external load was applied to a node of the truss structure, there was a relatively high initial stiffness until the load causes one of the beams to buckle, at which point the force exerted at the node markedly decreases, approaching a zero-stiffness regime. This behavior is like a mechanical fuse: During normal operation, the structure is relatively stiff, allowing functionality; yet, beyond some threshold force, it buckles, limiting damage to itself or the environment. The exact level of the threshold force could be tuned via control of the robot configuration, leveraging existing work on the mechanics of inflated beams (*47*–*49*). Because of its relatively high stiffness before buckling, the robot can carry heavy loads without substantial deformation. Figure 4C and movie S8 demonstrate the robot moving a 6.8-kg load over a trajectory. The kinematics model also allows us to predict the forces experienced by the members. Movie S9 shows the predicted axial load on each inflated member, while it changes shape in the presence of an external load similar to the experiment in Fig. 4C.

Different recovery strategies can be invoked after an inflated beam buckles. Occasionally, the beam will recover on its own when the load is removed. This is due to the small but noticeable restoring forces seen in Fig. 4B. If a beam is unable to recover passively, it is possible for active motions of the roller modules to assist in straightening buckled beams (movie S10).

The compliance of the robot allows it to grasp and manipulate objects. We demonstrate this behavior in Fig. 5A, as the robot changed shape to engulf an object (a basketball) before changing shape to pinch the object between two of its edges. The compliant beams bent slightly around the object, increasing the contact area. Once the object was grasped, it changed the shapes of its other faces to pick the object up from the ground. The robot could also manipulate objects "in hand," leveraging the fact that the edges are composed of continuous tubes that move relative to the nodes. In Fig. 5B, a basketball was placed between two edges of a tube. By driving the roller module closest to the basketball, the tube moved relative to the basketball, causing the ball to rotate within the grasp (movie S11).

Robot subcomponent analysis and design

The key components of our robot are the tubes and the actuated roller modules, shown in Fig. 1. Each roller module in the robot serves three primary functions: (i) to pinch the tube, creating a region of low bending stiffness—an effective joint; (ii) to locomote along the length of the tube, moving the position of the effective joint; and (iii) to mechanically couple to other roller modules in the structure in a way that fully defines the geometry of the robot.

Joint-like behavior of a pinched tube

The effective joints, about which two sections of tube pivot, are created by the cylindrical rollers in the roller modules. The rollers pinch the tube, reducing its cross-sectional area and bending stiffness while still allowing airflow. Ideally, there would be no torque required to change the angle, but in practice, there is a torque at these joints. To understand and minimize this torque, we developed a reduced order model. We assume that the fabric that makes up the pressurized tube is flexible yet inextensible and takes a shape that maximizes the enclosed volume, independent of its material properties or internal pressure. We relate the torque applied by the joint [$\tau(\theta)$] to the internal pressure P and the change in volume with angle

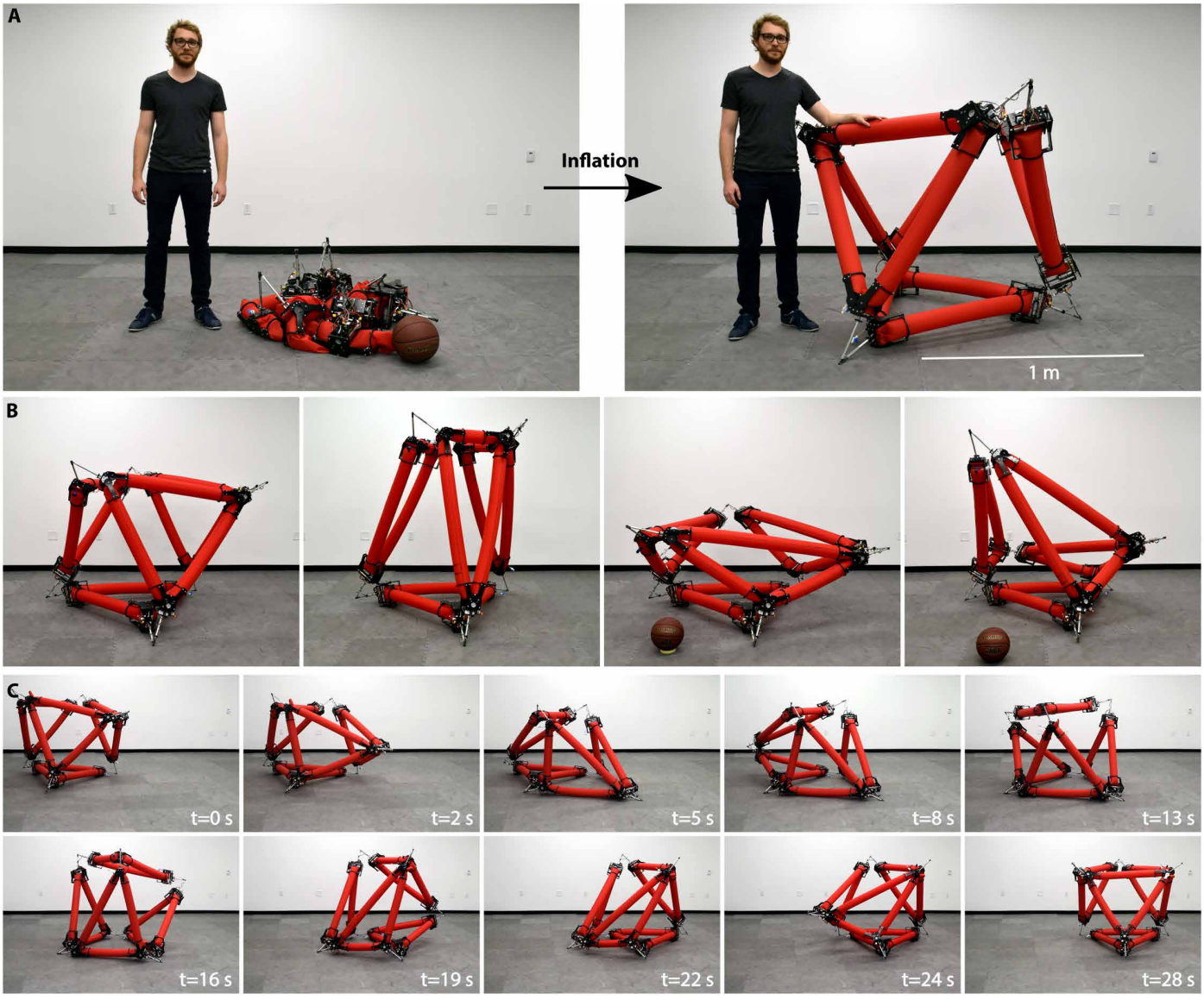

Fig. 3. A 3D untethered, octahedron truss robot capable of shape-morphing and locomotion. (**A**) The robot first inflates from a small package into an octahedron. The octahedron is composed of four individual triangles. (**B**) The robot can exhibit extreme shape change. A 186-cm-tall human and a 24-cm-diameter basketball are shown for size reference in some images. (**C**) The robot is also capable of a punctuated rolling gait, beginning with one of the four triangles as a bottom face (t = 0 s) and returning to this configuration (with a different triangle now at the bottom) after two rolling events (t = 28 s).

$\left(\frac{dV(\theta)}{d\theta}\right)$ using the principle of virtual work through $\tau\left(\theta\right) = -P\frac{dV(\theta)}{d\theta}$ (see Supplementary Text and fig. S2).

To validate the model, we gathered data using the test setup shown in fig. S2C and compared them with predictions from the model (Fig. 6). The data show that at small angles, torque increases with roller diameter (Fig. 6A) and tube diameter (Fig. 6B). At a certain angle, the two sections of tube collide with one another, and the torque increases rapidly, as illustrated in Fig. 6A. We terminated the predictions at the onset of this interference, which occurs at a larger angle with increased roller diameter and a smaller angle with increased tube diameter. The model captures the shape of the curve until interference occurs, although it slightly underpredicts the resulting force. This could be because it accounts only for the response of the air and not for the resistance of the fabric tube to bending.

Examining the trends from Fig. 6 (A and B), it is ideal to use small rollers to reduce the torque associated with the tubes pivoting about the effective joint but use large rollers to avoid the self-interference of the tube. To address these competing objectives, we introduced a design that uses two pairs of rollers as shown in Fig. 6C. In this way, we gained the low-torque performance of the small rollers while also avoiding the self-interference that markedly increases torque (Fig. 6D).

Locomotion along an inflated tube

The second requirement of the roller module is to continuously move the joint along the structure, which it does by rotating the rollers with a motor. Because the gap between the rollers is smaller than the diameter of the tube, the rollers experience a high normal force pushing them apart (see Supplementary Text and fig. S3 for further analysis). This, when coupled with a high-friction coating on the

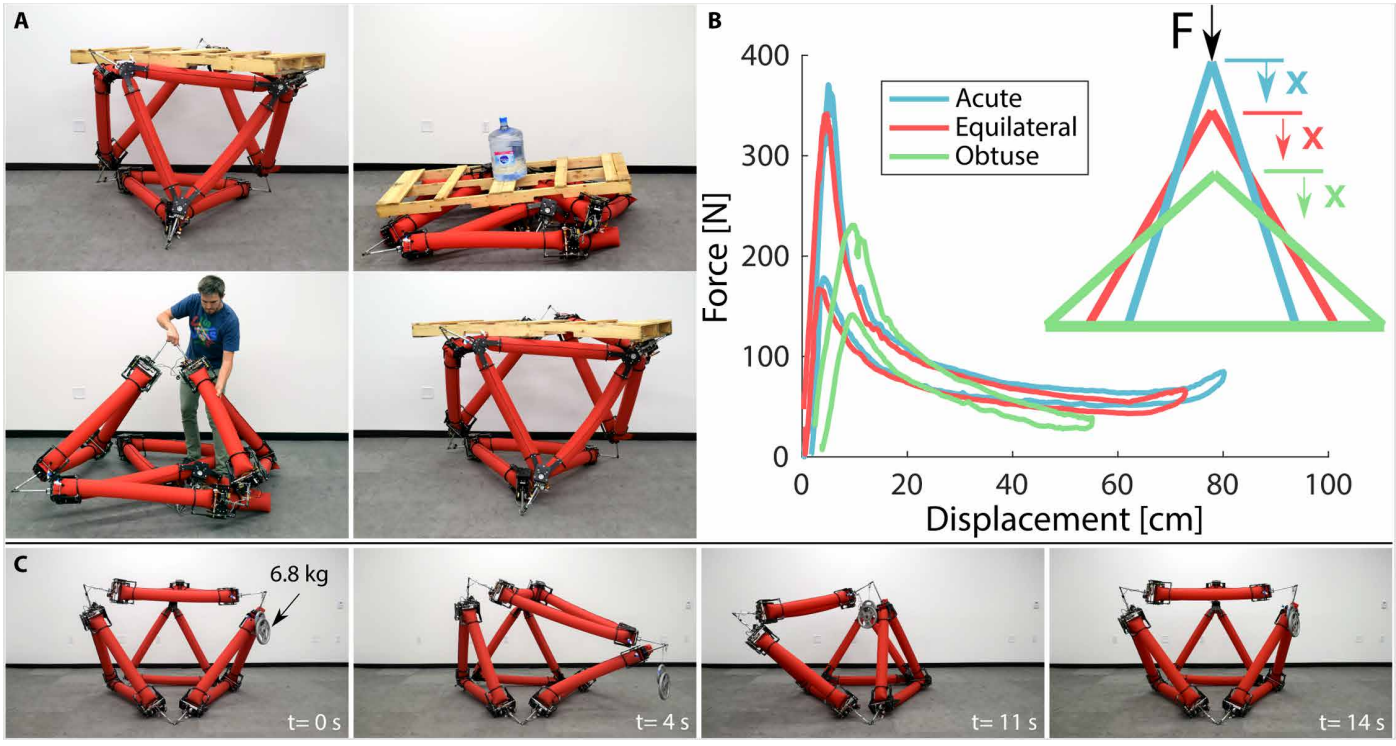

Fig. 4. Demonstration and characterization of the robot's compliant behavior. (**A**) Overloading the robot causes the robot to collapse. After being restored to its initial configuration, the robot is again able to support the initial load. (**B**) Load displacement behavior of a single triangle in three different configurations. In all cases, there is a moderate initial stiffness until a critical load is reached and the beam buckles, at which point the force required to maintain a given level of deflection is much lower than the peak value, demonstrating a mechanical fuse–type behavior of the robot. (**C**) The robot moves a 6.8-kg load over a trajectory.

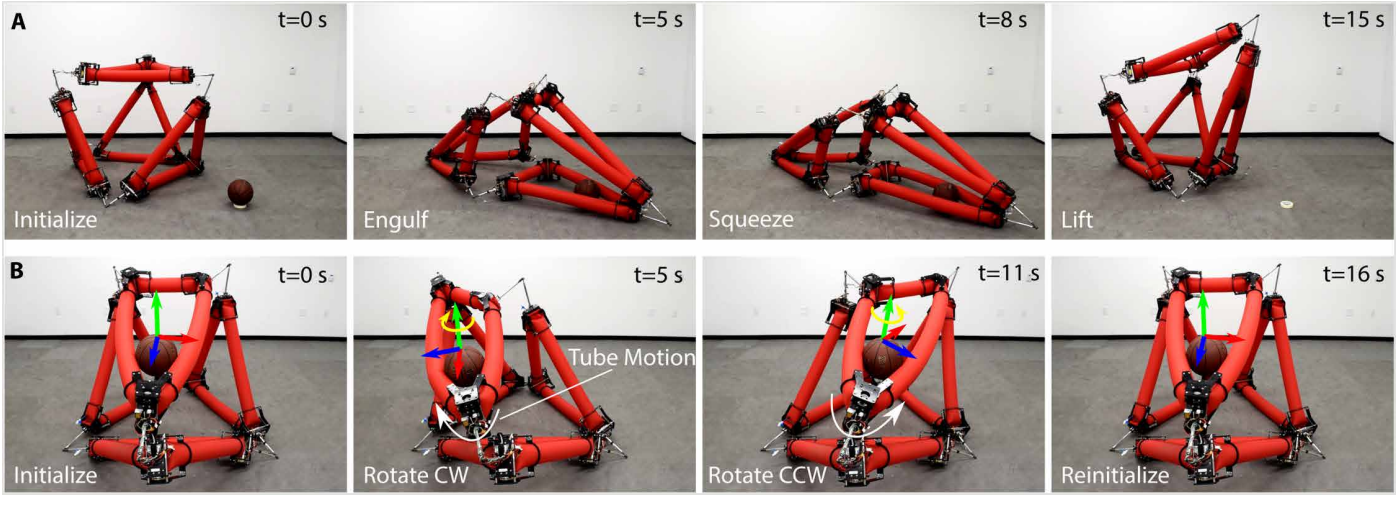

Fig. 5. Demonstration of the robot's ability to use its inherent compliance to manipulate and interact with objects. (**A**) The robot grasps a basketball (diameter of 24 cm and mass of 580 g) by first engulfing it and then pinching it between two compliant edges. The robot then changes shape to lift the basketball into the air. (**B**) With the basketball secured between two edges, motion of the roller module closest to the basketball causes the basketball to spin. A coordinate frame has been added to allow visualization of how the orientation of the basketball changes. Between the second and third configurations, the basketball rotates about 135°. CW, clockwise; CCW, counterclockwise.

cylinders, ensures a large friction force between the tube and the rollers and prevents slip.

In an ideal case, the energetic cost to move the roller along the tube would be zero and invariant to changes in the internal pressure of the system. However, the presence of friction and hysteresis in the deformation of the fabric results in an energetic cost to travel a distance, which we seek to minimize.

To measure the cost to move in the presence of the non-idealities, we used the experimental setup shown in Supplementary Text and fig. S4. The first test examined the effect of roller diameter and internal

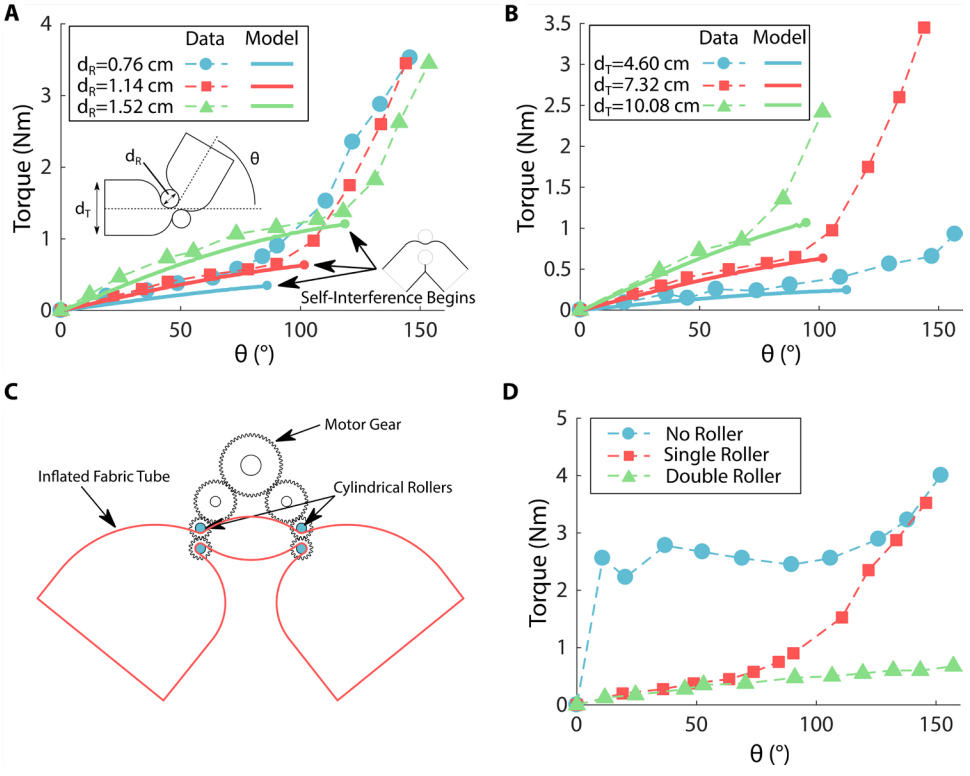

Fig. 6. Analysis of the effective joint formed by rollers pinching a tube. (**A**) The relationship between angle and torque with changing roller diameter (tube diameter is 7.32 cm). Model predictions are shown in solid lines, and experimental data are shown in dashed lines. The model slightly underpredicts the torque. The amount of torque increases substantially beyond the point where the model predicts self-interference. Torque increases with roller size, but interference also begins at larger angles. (**B**) Increasing torque with increasing tube diameters when the roller diameter is 1.14 cm. (**C**) Double roller configuration and the gear train that ensures all rollers move together from a single motor input. (**D**) Torque required to bend a tube with no rollers, with a single set of rollers, and with two sets of rollers as shown in (C) (roller diameters are 0.64 cm separated by 6.35 cm). Without rollers, the tube exhibits low stiffness, but large torque at a wide range of angles. The presence of one set of rollers markedly reduces the torque at low angles, but the torque rises quickly after self-interference begins. With two sets of rollers, the torque is low for small and large angles because the tube does not self-interfere.

pressure on the force required to move tubes through a pair of rollers, where the tube has a diameter of 7.32 cm. We found a linear relationship between force and pressure (Fig. 7A). The diameter of the roller had a small effect on the slope of these lines, with the largest rollers having the largest slope.

In the second test, we measured the effects that the internal pressure and tube diameter have on the force required to move tubes through a pair of rollers 1.14 cm in diameter. We observed that increases in pressure and tube diameter both increase the force to move (Fig. 7B). This is because both factors result in a larger normal force on the rollers, and a larger diameter tube results in more material being deformed through a larger motion.

In the third test, we compared the cost to move of a single set of rollers to that of two pairs of rollers separated by a variable distance. In Fig. 7C, we show that the cost to move for two pairs of rollers was less than twice that for one roller. Note that we tested roller spacings less than a diameter of the tube because spacing greater than a diameter is not effective at reducing joint torque and is thus not practical.

To gain a sense of the relative magnitude of the forces required to move the tube through the rollers, we compared the measured force with the maximum force that could be exerted by the pressurized air, calculated as pressure times the cross-sectional area of the tube. Across all of the data shown in Fig. 7, the forces required to move the tube through the rollers had a peak of 14.6% and a mean of 8.78% of the maximum force, indicating that the forces required to move the tube through the rollers are small in comparison.

Having examined the geometric effects on joint stiffness and the cost to move, we can make some design decisions. Using smaller rollers reduces the joint stiffness (Fig. 6A) and decreases the cost to move (Fig. 7A). Therefore, using small rollers is preferable for performance. Increasing the spacing between the pairs of rollers not only decreases the minimum angle before tube interference but also increases the cost to move. For our roller modules, we selected a roller diameter of 0.76 cm and set the distance between the center axis of the rollers at 1.27 cm. The distance between the two pairs of rollers was 6.35 cm. In practice, we drove both sets of rollers with a single motor through the gear train shown in Fig. 6C.

Roller connections

The third requirement of the roller module is the ability to mechanically couple to other roller modules in the structure to fully define the robot's geometry for both 2D and 3D architectures. The roller modules connect to each other at nodes using three-degree-of-freedom universal joints that are composed of a clevis joint that couples two rods, each free to spin about its axis (Fig. 1D). The length of these rods is determined by the size of the roller modules and the necessary minimum angle between these rods.

The mechanical design of the roller modules and the connections between them must fully constrain the truss structure. Fully constrained means that any external load induces a restoring force that seeks to return the structure back to an equilibrium configuration. Our kinematic analysis (see Materials and Methods) indicates that the structure is fully constrained if the connection point between a roller module and its neighbor lies along the line that bisects the two segments of tube joined by that roller. To achieve this constraint, we included two guide rings as shown in fig. S6. Each guide ring was attached to the body of the roller module through arms that rotate about a pin joint concentric with the top roller in a pair of rollers. In addition, we placed gear teeth on the arms supporting the guide rings to couple the motion of the guide rings. We call these arms geared angle constraints (fig. S6). Together, the guide rings and the geared angle constraints ensured that a central axis of the roller module bisects the two segments of tube, which, in turn, ensured that the truss structure is fully constrained.

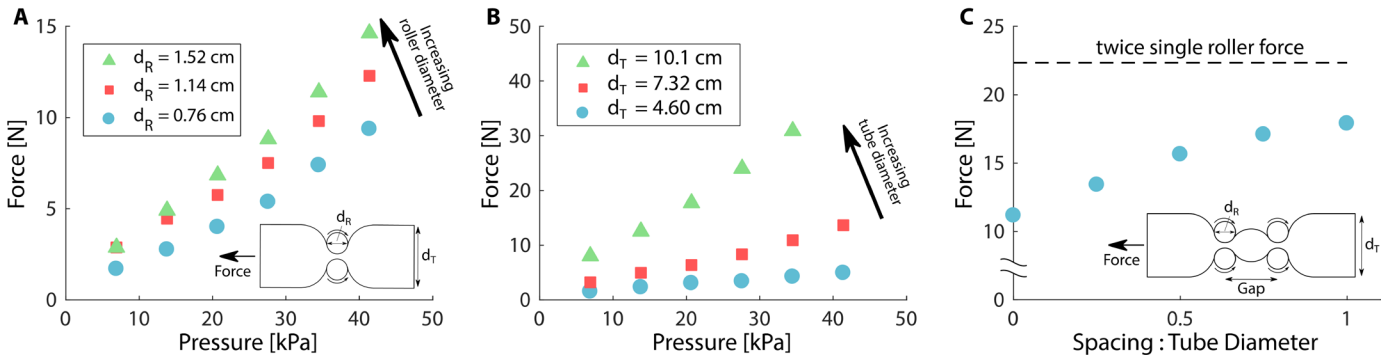

Fig. 7. Exploration of the energetic cost to move along the tube. (**A**) Force required to move the tube through the rollers over a range of pressures and with three different roller diameters. The tube diameter is 7.32 cm. The force-pressure relationship is approximately linear, and increasing the roller diameter slightly increases the required force. (**B**) Force required to move the tube through the rollers over a range of pressures and with three different tube sizes. The roller diameter is 1.14 cm. The force-pressure relationship is approximately linear, and tubes with larger diameter require more force. (**C**) Force required to move a 10.1-cm tube at 30 kPa through two pairs of 0.76-cm rollers over a range of distances between the pairs. A single roller is included with gap distance equal to zero. The double roller cost to move when the separation is equal to the tube diameter is 80% of twice the single roller cost to move.

Tradeoffs: Workspace, efficiency, and speed

We now discuss the tradeoffs inherent in the isoperimetric robot design and compare this robot to truss and pneumatically actuated robots. In the first set of comparisons, we examined the effect of kinematic differences between an isoperimetric robot and a conventional truss robot on their respective workspace. Next, we analyzed how these kinematic differences affect efficiency and speed of movements. In the last set of comparisons, we examined the effect of the power source—electric motors for the isoperimetric robots and microcompressors for pneumatically actuated robots—on efficiency and speed.

Effects of kinematic differences on workspace

We qualitatively then quantitatively compare the workspace of a conventional truss robot with that of our robot. Qualitatively, in the conventional truss robot, each edge is a linear actuator with a fixed amount of material that is locally reconfigured to change the edge length. In our robot, each edge can exchange material with other edges to change length. This reallocation of material is conceptually similar to changing the shape of a fixed mass of clay: The shape can change markedly, but the total amount of material must remain the same. In many cases, our concept allows for larger extremes in the length of an individual edge than does a conventional truss robot. However, it also necessitates coupling for changes in the length of edges that are part of the same tube. Each individual tube in the architecture represents another constraint on the achievable configuration space and a potential reduction of the workspace. As a result, an isoperimetric robot will have fewer degrees of freedom than a robot composed of linear actuators with the same graphical structure. Therefore, some motions that are possible for a conventional truss robot are impossible for our robots. The octahedron robot, for example, cannot reduce its total edge length to become a smaller regular octahedron, although its enclosed volume can substantially change. The mathematical form of these constraints is discussed in the "Kinematics" section (see Materials and Methods).

Next, we quantitatively compare the reachable workspaces of the top node of three different 2D triangular robot architectures: an isoperimetric robot with two active roller modules, a conventional truss robot with a linear actuator on each edge, and a conventional truss robot with linear actuators on two edges and supported by two pinned nodes (Fig. 8 and movie S12). The workspace of our robot completely covers the workspace of the robot composed of three linear actuators, which, in turn, completely covers the workspace of the robot composed of two linear actuators. The workspace of our robot is 3.4 times larger than the workspace of the robot composed of three linear actuators and 6.8 times larger than the workspace of the robot composed of two linear actuators. These results indicate that, in some cases, the isoperimetric architecture may increase a robot's workspace.

Effects of kinematic differences on efficiency and speed

We first qualitatively, then quantitatively, compare how the kinematics of an isoperimetric robot and a truss robot affect the efficiency and speed of motion. Qualitatively, the added constraints on the isoperimetric robot mean that certain motions require much more energy or must be performed more slowly than others—a factor that should be considered when planning movements. This can be explained as follows: Unlike in a truss robot, the number of actuators (for our robot, roller modules) needed to change the robot's configuration is not necessarily equal to the number of edges that are changing in length. For example, exchanging length between the two edges adjacent to the same active roller module (edges 1 and 2 in Fig. 8A) requires only the energy to operate one roller module. However, exchanging length between edges separated by multiple active roller modules (edges 1 and 3) requires multiple roller modules to drive. These effects are exacerbated if a single tube covers more than three edges in a triangle, as illustrated in Fig. 2 (D and E). The coupling between edge length changes and the routing of the tube also affects the rate of change of different edge lengths. For the robot in Fig. 8A, edge 2 can lengthen at twice the maximum speed of the rollers and hence twice the maximum speed of edges 1 and 3 due to the fact that it has active rollers on both ends. However, it can only extend at maximum speed if both edges 1 and 3 are contracting at the maximum speed. These dependencies illustrate that the energy required to perform a given motion and the speed at which edge lengths can change depend on the architecture of the graph, not just the parameters of the actuators as in a truss robot composed of linear actuators.

We quantify these differences by comparing the motions of the robots in Fig. 8. Figure 8D shows the manipulability index, μ (*50*), for node 2 throughout the two robots' respective workspaces. The manipulability index is the volume of the manipulability ellipsoid that represents the node velocity resulting from normalized actuator

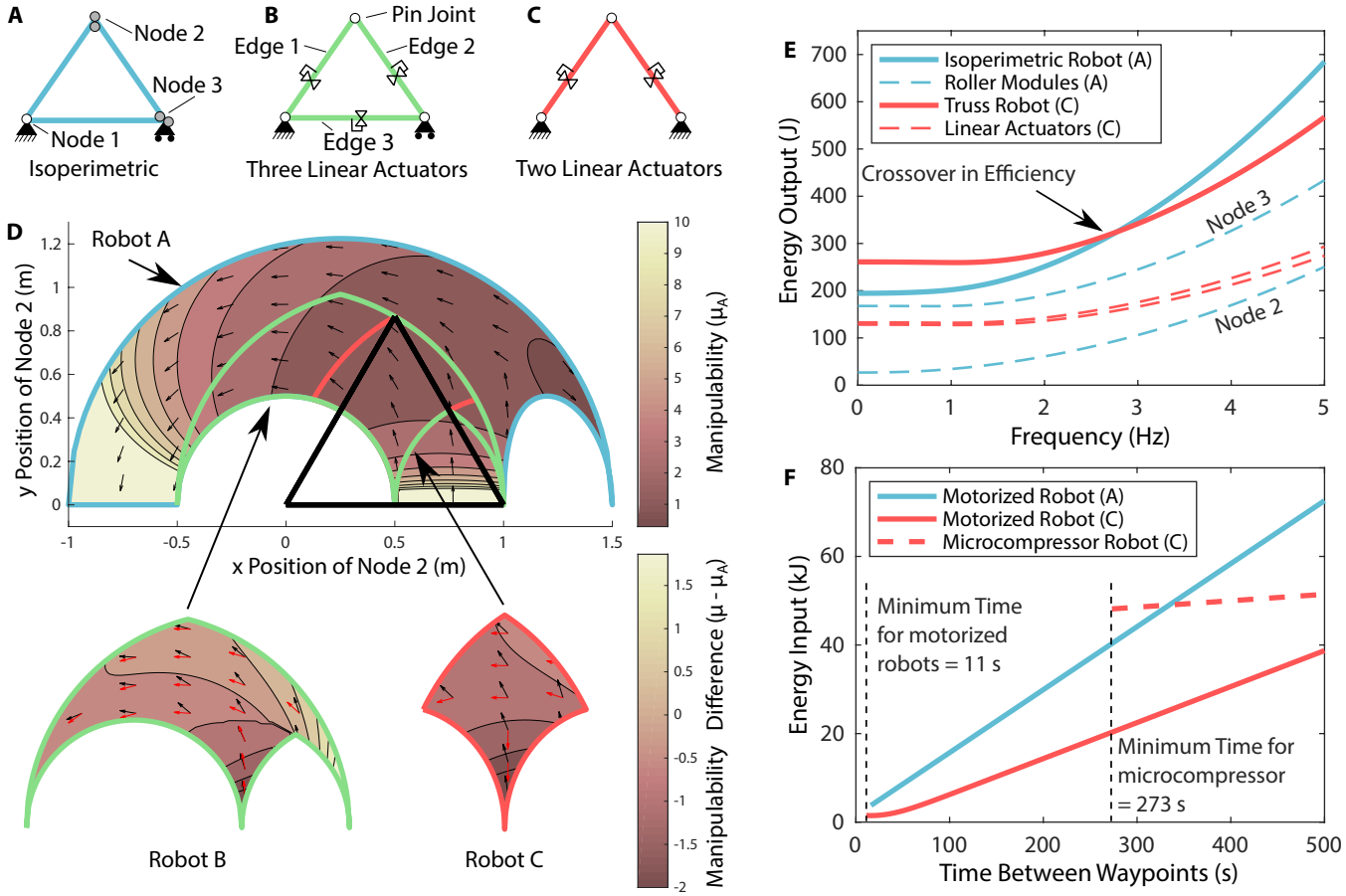

Fig. 8. Comparison of 2D triangular robot architectures. (**A**) Isoperimetric robot. (**B**) Truss robot with three linear actuators. (**C**) Truss robot with two linear actuators. (**D**) Workspaces and manipulability index, μ, of node 2 for each robot. The minimum edge length for all robots is 0.5 m, and the maximum length of linear actuators in robots B and C is 1 m. The total edge length of the isoperimetric robot is the maximum perimeter of the truss robots (3 m). The small black and red arrows indicate the direction of maximum velocity for node 2 of robot A and robots B and C, respectively. (**E**) Effect of frequency on the energy required to move node 2 between 50 waypoints within the shared workspace for robots A and C. With increased frequency, the isoperimetric robot becomes less efficient because of the coupled motion of nodes 2 and 3. (**F**) Required energy to move node 2 between waypoints when both robots A and C are driven by a specific electric motor and when robot C is driven by a microcompressor of comparable mass. The systems driven by an electric motor are faster than those driven by the microcompressor.

inputs. Larger manipulability indices correspond to larger end effector motions given fixed actuator inputs. The manipulability index is higher for the isoperimetric robot than the robot with two linear actuators across the shared workspace, indicating the possibility of faster motions, but with the corresponding result that higher actuator torques are required to resist external loads. For the robot with three linear actuators, the robot has redundancy to the task of positioning node 2, which we exploit to maximize the manipulability. Even so, the isoperimetric robot has higher manipulability in a portion of the shared workspace. To further examine this effect, we examine the energy required to move node 2 of robots with two degrees of freedom (A and C) between a set of randomly generated waypoints while the robot is subject to gravitational and inertial loads (details in Supplementary Text and fig. S8). The energy output is slightly lower for the isoperimetric robot for low-frequency motions. However, as the frequency of motion increases, the required output energy increases faster for the isoperimetric robot than for the truss robot (Fig. 8E). For a prescribed motion of node 2, node 3 of the isoperimetric robot must also move to maintain the constant perimeter. The additional motion of node 3 is increasingly costly as frequency increases and dynamic effects become more pronounced. Furthermore, the individual contributions to output energy from the linear actuators are nearly identical. Meanwhile, one of the roller modules in the isoperimetric robot exerts much more energy than the other. These results indicate that the coupled nature of motion in isoperimetric robots creates tradeoffs in both speed and efficiency.

Effect of power source on efficiency and speed

Last, we compare efficiency and speed of different robots based on their use of either electric motors or microcompressors as an energy source. We compared robot A driven by electric motors with two different types of robot C: one of linear actuators driven directly by electric motors and one of pneumatic cylinders driven by microcompressors (details in fig. S8). In this comparison, we used commercially available components to investigate the qualitative characteristics of these devices. We cannot assume that the quantitative results will apply to all commercially available components or reveal fundamental limitations of these technologies. We found that robot A is less efficient than the motorized robot C (Fig. 8F), despite the energy output advantages seen in Fig. 8E. This is due to the uneven distribution of load among the two actuators. We found that the minimum time in

which the microcompressor-driven robot C can move between waypoints is much slower than the motor-driven robots, yet it is potentially more efficient at low speeds. However, we observed that the time to execute trajectories for the microcompressor-driven robot C depends heavily on the diameter of the pneumatic cylinder considered. Increasing the size of a robot driven by a microcompressor increases the area the compressed gas exerts a pressure on, effectively increasing the gear ratio: This increases the force output and reduces the speed. This effect is observed in the untethered soft robot presented in (*6*). The authors built their robot at a relatively large scale (length of 0.65 m) to accommodate commercially available compressors. The increase in size to accommodate commercial components had the effect of reducing speed (reported speeds of about 18 m/hour or 28 body lengths/hour). Our robot is larger, but, because it does not experience the same effect of gear ratio change, it achieves faster locomotion speeds (216 m/hour or 128 body lengths/hour).

DISCUSSION

In terms of softness, our robots differ from most devices in the field of soft robotics. Although our robots are like most soft robots in that they comprise a mixture of compliant materials (fabric and air) and some rigid components, they differ in that their rigid components are external instead of internal. At first glance, this may seem limiting, but it is a similar architecture to that found in insects, where rigid exoskeletal segments are joined by compliant tissue (*51*). In our case, the natural compliance of the beams connecting the rigid nodes creates an effective stiffness that is far below the actual stiffness of node material. Further, the mechanical fuse–type behavior limits the overall maximum load that can be applied at a node. Naturally, the compliant tubes afford some robustness to the roller modules because the tubes can conform to misalignment of the rollers and prevent large forces and impacts from being transmitted between roller modules. In addition, it may be possible in future work to replace the roller modules with soft-bodied analogs to further increase the safety and robustness of the system.

In this work, we presented versions of our robot at an approximately human scale. A key question for understanding the broader applicability of this type of robot is how performance changes with robot size scale. If we scale all dimensions uniformly, then as the length L increases, the mass of the robot increases roughly with L^3. The strength of the structure is governed by the mechanics of inflated beams and is a function of the geometry, material properties, and internal pressure, which precludes extracting a simple scaling law. If we assume that the strength of the structure can be approximated by considering the inflated tubes as Euler beams that fail due to buckling, the load-bearing capacity increases with L^2, a slower rate of increase than the robot's mass, meaning that isometric upscaling will eventually result in robots that cannot support their weight. However, given that buckling strength depends on the fourth power of tube diameter, slightly positive allometric scaling of tube diameter would enable increased robot sizes.

We envision a variety of potential applications for robots based on our concept. For example, in planetary rover missions, a robot using our architecture could deflate and pack in a small volume for launch, inflate upon landing, and then perform missions untethered from any energy source. The soft nature of the robot would enable robustness, and the robot could change its shape to navigate challenging terrain or perform tasks that may not be known a priori. The compliance and shape change of the robot could make it suitable for several tasks involving humans. For example, the robot could work alongside workers, holding parts in place as the worker bolts them in place. In the classroom, the modularity and soft nature of the robotic system make it a potentially valuable educational tool. Students could create many different robots with a single collection of hardware and then physically interact with the robot. By including a much larger number of roller modules in a robot, the robot could function as a shape display, dynamically changing shape as a sort of high–refresh rate 3D printer (*52*). Incorporating touch-sensitive fabric into the structure could allow users to directly interact with the displayed shapes. More broadly, the modularity allows the same hardware to build a diverse family of robots—the same roller modules can be used with new tube routings to create new robots. If the user needed a robot to reach through a long, narrow passageway, they could assemble a chain-like robot; then, for a locomoting robot, they could reassemble into a spherical shape.

Our robotic concept is built upon a synthesis of concepts from collective, truss-like, and soft robots. We demonstrated its collective nature by creating—from identical, one-degree-of-freedom subunits—two 2D architectures and one 3D architecture. We showed the robots' truss-like behavior through marked shape change, load carrying, and locomotion. We demonstrated and characterized their compliant nature through a mechanical fuse behavior and an ability to engulf, grasp, and manipulate objects. Beyond these demonstrations, we presented an analysis for the design of robot subcomponents. We developed and validated a model that predicts the stiffness of a joint formed by a roller modular and experimentally studied the effect of geometric parameters on the force required to drive a roller along the tube. Last, we examined tradeoffs, comparing the workspace, efficiency, and speed of a robot based on our concept to these characteristics of similar robots. Our work introduces the isoperimetric concept to the field of soft robotics for the structure and movement of untethered pneumatic robots.

MATERIALS AND METHODS

Construction

The inflatable tubes we used in our demonstration were constructed out of an outer layer of heavy fabric and an inner air-tight bladder. We selected a commercially available fabric with minimal stretch along the 45° bias. This fabric is a 200-denier nylon fabric with an oxford weave and a urethane coating (Seattle Fabrics Inc.). The fabric was cut into a long rectangular piece and sewn together with a plain seam and a straight stitch. A small hole was punched into the fabric for a pressure line connector. The inner bladder was formed from a low-density polyethylene tube (Hudson Exchange). This tube was cut to length, a hole was punched in its side for the fitting, and the ends were heat-sealed. The inner bladder was inserted into the fabric outer layer, and the ends of the outer layer were sewn shut with a straight stitch. Last, a threaded through-wall pipe fitting was fastened in place where the holes in each layer aligned. In practice, we inflated the tubes to about 40 kPa.

The housing of the roller module was created with laser-cut polyoxymethylene sheets. These pieces were fastened together with standoffs and corner brackets. The housing contained holes to lightly press fit ball bearings that support the rotation of the rollers and the gear train. The rollers were steel D-shafts wrapped in a nonslip material (Dycem). External grooves were cut into the rollers, where retaining

rings were placed to locate the rollers with respect to the ball bearings. The custom gear train had a speed multiplier of 3, which was selected for geometric convenience. Our gear train was driven by a direct current motor with a planetary, reducing gear box with a gear ratio of about 139:1 (ServoCity #638320). The motor was driven by a Cytron MD10C motor driver in a drive-brake control method. The motor driver was commanded by a Teensy 3.2 microcontroller, which used an nRF24l01+ radio transceiver to receive position commands from an off-board laptop. The laptop was not a necessary component because the position commands could be stored on the microcontroller. The laptop provided a convenient user interface to send commands to the microcontrollers. When multiple roller modules were connected at a vertex, a single microcontroller controlled all the connected roller modules. When possible, we connected passive modules together to reduce the number of microcontrollers. Power was delivered to each roller module by a 1300-mAh, 75-C, 14.8-V lithium polymer battery manufactured by Tattu. The mass of each roller module was 2.83 kg, and each passive module weighed 1.6 kg. The complete octahedron robot (eight active roller modules, four passive modules, and the fabric tubes) weighed about 29 kg. The 2D robots weighed 22 kg (three tubes) and 19 kg (single tube). A part callout for the roller module is shown in fig. S6.

Control

Each roller module was responsible for controlling its position in 1D along the inflated tube. The microcontroller tracked the position of the connected roller modules along their tubes using the motor encoders and used a proportional-integral-derivative (PID) controller to drive the rollers to the target position. To determine the desired commands to broadcast to the robot, we experimented with different commands using a computer simulation that propagated the kinematics presented in the next section.

Kinematics

Understanding the kinematics of the system allowed us to analyze and control the robot's motion, as well as understand the forces the actuators must apply during operation, and informed what types of physical constraints we must include in the mechanical design of the roller module. We first present the kinematics relating the motion of the roller modules to the position of the nodes in the idealized case where the center axis of each edge intersects exactly at the joints of the structure. We then expand this treatment to discuss the kinematics of the structure when the effective centers of rotation do not coincide with the joints, as is a physical necessity of the robot. The kinematics of a network of linear actuators connected into an arbitrary structure are presented in (*53*). We summarize the key results from that work here and extend the kinematics to the case of a robot where several edges are composed of a single tube.

Idealized kinematics

We model the robot as a framework, a mathematical structure that consists of a graph G and vertex positions $p_i \in \mathbb{R}^d$. The graph is denoted as $G = \{V, E\}$, where $V = \{1, \ldots, n\}$ are the vertices of the graph and $E = \{\{i,j\}_1, \{i,j\}_2 \ldots \{i,j\}_{N_L}\}$ are the undirected edges of the graph. The geometry of the robot (assuming no deflection of the members) is fully represented by the concatenation of all vertex positions $x = \left[p_1^T, p_2^T, p_3^T, \ldots p_N^T\right]^T$. The length of each edge can be obtained

$$L_k = \|p_i - p_j\| \forall \{i,j\}_k \in E \tag{1}$$

We form the differential kinematics that relate the changes in the edge lengths to the changes in the node positions as follows

$$\frac{dL_k^2}{dt} = 2 L_k \dot{L}_k = 2 (p_i - p_j)^T \dot{p}_i + 2 (p_j - p_i)^T \dot{p}_j \tag{2}$$

Rearranging this into matrix form, we obtain

$$\dot{L} = R(x) \dot{x} \tag{3}$$

We also express the constraints that ground the robot to the outside world in the form

$$C\dot{x} = 0 \tag{4}$$

where C is a matrix that constrains the structure to the outside world. In practice, we identify three ground nodes of the robot and pick C such that one ground node is fixed in all directions, the second is fixed in two directions, and the third is fixed only in the direction normal to the ground. Combining Eqs. 3 and 4, we obtain

$$\begin{bmatrix} \dot{L} \\ 0 \end{bmatrix} = \begin{bmatrix} R(x) \\ C \end{bmatrix} \dot{x} \tag{5}$$

If $[R(x)^T C^T]^T$ is invertible, then we find the forward kinematics (Jacobian) that relates the rate of change of the actuator edges to the motion of the nodes

$$\dot{x} = \begin{bmatrix} R(x) \\ C \end{bmatrix}^{-1} \begin{bmatrix} I_{N_L} \\ 0 \end{bmatrix} \dot{L} = J_L(x) \dot{L} \tag{6}$$

The matrix $[R(x)^T C^T]^T$ is invertible when the robot is minimally infinitesimally rigid, which intuitively means that the robot has the minimum number of edges to ensure static independence and that each edge is capable of changing length independently. For the matrix to be square and invertible, the number of edges in the network must be $3n - 6$ for the 3D robot and $2n - 3$ for the 2D robot. Using the well-known relationship between the Jacobian and externally applied forces, we write

$$J(x)^T F = \tau_L \tag{7}$$

where τ_L is the vector of forces on the linear actuators and F is a vector of forces applied at the nodes.

We now incorporate the constraints that several of the linear members in the robot are composed of a single tube and that their total length must remain constant. In our treatment, we will assume that the paths defined by the tubes each form a cycle, meaning that they begin and end at the same node. This allows us the mechanical convenience of connecting the beginning and end of the tube at a passive module. Including paths that start and end at different nodes requires only minor modification. The path of the tube or tubes through the robot is defined by an ordered pair of nodes, where each stop at a node corresponds with a roller module, which we number 1 to N_{roller}. We represent these paths as a matrix $B_{\text{all}}(G) \in \mathbb{R}^{N_{\text{roller}}, N_L}$. Each column of B_{all} corresponds to one edge of the graph and has exactly two nonzero entries: a 1 in the row corresponding to the tail node of the directed edge and a −1 at the row corresponding to the head of the directed edge. This matrix allows us to relate the velocity of the rollers to the rate of change of the edge lengths

$$\dot{L} = {B_{\text{all}}}^T \dot{\theta} \tag{8}$$

where θ corresponds to the position of each of the rollers along the tube. To relate the motion of the rollers directly to the motion of the nodes, we combine Eqs. 6 and 8 to obtain

$$\begin{bmatrix} R(x) \\ C \end{bmatrix}^{-1} \begin{bmatrix} {B_{\text{all}}}^T \\ 0 \end{bmatrix} \dot{\theta} = \dot{x} = J_\theta(x)\,\dot{\theta} \tag{9}$$

The Jacobian $J_\theta(x)$ relates the motor motions to node motions, which also allows us to quantify the torque required from the motors to hold a particular configuration as $\tau_{\text{roller}} = J_\theta(x)^T F$.

We note that the sum of all of the edge lengths of the structure is obtained as $1^T L$. We can confirm that the total length of the shared member is unchanged for any combination of roller velocity inputs by showing that $1^T B^T = 0$, which is a result of the construction of the B matrix, as we have ensured that each column sums to 0.

If each tube in the robot is a single continuous loop with no end, all the roller modules could run at the same speed and the tube would move continuously, while all the nodes remain stationary, as indicated by the fact that $B^T 1 = 0$. In practice, we do not include a motor at the node that makes up the first and last connection for each tube, which corresponds to removing the elements of $\dot{\theta}$ and columns of B that correspond to the first and last node of each tube in the robot.

Kinematics in the presence of offsets

In practice, it is not possible for the edges to intersect at the nodes due to the large size of the tubes and the double-roller design of each roller module (Fig. 6C). In the presence of these offsets, we represent the kinematic state of each roller module as the position of three points. These points are illustrated in fig. S7 and are the point where two roller modules connect (denoted point A) and the point at the center of each pair of rollers in plane with the inflated tube (points B and D). We denote the point at the opposite end of each tube segment from points B and D as points C and E, respectively. We want to impose sufficient constraints in the physical design of the roller module so as to fully constrain the kinematic state of all roller modules (points A, B, and D for each module). For a robot in 3D, each new point introduced into the kinematic state introduces three new degrees of freedom. For each roller module, we must remove six degrees of freedom. We have chosen to include two guide rings that are geared together such that they, along with the mechanical construction of the roller module, enable the following mathematical constraints:

1) All edges in the triangle formed by points A, B, and D are constant length. The resulting forces are provided by the physical structure of the roller module. This imposes three constraints that are of the same form as the constraints in Eq. 1. We take the derivative of these constraints and rearrange them into the matrix $R_{\text{node}}(x)$.

2) A constraint that the angle CBD is equal to the angle EDB. This constraint is provided by gear teeth that are included onto the arms of the angle constraint shown in fig. S7. This imposes one constraint, which is expressed

$$\frac{(x_d - x_b)^T (x_c - x_b)}{\|x_d - x_b\| \|x_c - x_b\|} = \frac{(x_e - x_c)^T (x_b - x_c)}{\|x_e - x_c\| \|x_b - x_c\|} \tag{10}$$

We take the derivative of this constraint for each roller module in the network and put the result into the matrix $R_{\text{bisect}}(x)$.

3) A constraint that point A remains in the plane defined by points B, C, and D and the plane defined by points B, C, and E. This constraint requires coupling between the edges and the rollers in a direction normal to both edges. This imposes two constraints, which are enforced by the guide rings. This constraint is only necessary when the robot is in 3D. This constraint is expressed

$$\frac{(x_a - x_b)^T ((x_c - x_b) \times (x_d - x_b))}{\|x_d - x_b\| \|(x_c - x_b) \times (x_d - x_b)\|} = 0 \tag{11}$$

and

$$\frac{(x_a - x_c)^T ((x_b - x_c) \times (x_e - x_c))}{\|x_e - x_c\| \|(x_b - x_c) \times (x_e - x_c)\|} = 0 \tag{12}$$

We again take the derivative of each of these constraints in the current configuration and put the result into the matrix $R_{\text{planar}}(x)$.

We combine these results to form the following result

$$\begin{bmatrix} R_{\text{tube}}(x) \\ R_{\text{node}}(x) \\ R_{\text{bisect}}(x) \\ R_{\text{planar}}(x) \\ C \end{bmatrix} \dot{x} = \begin{bmatrix} \dot{L}_{\text{tube}} \\ 0 \end{bmatrix} \tag{13}$$

By including the constraints we have specified, we ensure that this combined matrix is square. If this matrix is of full rank (which is a function of the current node positions), then the overall structure is infinitesimally minimally rigid, and the structure cannot move relative to itself without violating the constraints. If the matrix is invertible

$$\dot{x} = \begin{bmatrix} R_{\text{tube}}(x) \\ R_{\text{node}}(x) \\ R_{\text{bisect}}(x) \\ R_{\text{planar}}(x) \\ C \end{bmatrix}^{-1} \begin{bmatrix} B^T \\ 0 \end{bmatrix} \dot{\theta} = J_{\theta,\text{full}}(x)\,\dot{\theta} \tag{14}$$

We can also extract the axial loads on the different members through $\tau_L = J^T_{\theta,\text{full}}(x)\,F$. We note that these are the resulting forces assuming that the edges are rigid. In practice, the compliance in the inflated tubes may alter the actual configuration and loads. However, this method generates a reasonable estimate of the loading conditions on the inflated tubes and the torques that must be exerted by the motors.

SUPPLEMENTARY MATERIALS

robotics.sciencemag.org/cgi/content/full/5/40/eaaz0492/DC1

Text

Fig. S1. Experimental setup for measuring battery life.
Fig. S2. Torque angle relationship for a beam between rollers.
Fig. S3. Model predictions of the normal force between rollers.
Fig. S4. Test apparatus to quantify cost of motion.
Fig. S5. Deformation of an individual triangle.
Fig. S6. Mechanical design of roller module.
Fig. S7. Diagram of points used to define the kinematics of each roller module.
Fig. S8. Details of the comparison with different truss robots.
Movie S1. Motion of the roller module along an inflated tube.
Movie S2. Inflation and shape change of a 2D robot.
Movie S3. Operation of a single-tube 2D robot.
Movie S4. Shape change of octahedron robot.
Movie S5. Comparison of predicted and measured motion.
Movie S6. Octahedron robot locomotes with a punctuated rolling gait.
Movie S7. Compliance and interaction of the robot with people.
Movie S8. Octahedron robot moving a payload.
Movie S9. Simulated loading with payload.
Movie S10. Self-recovery from buckling.

Movie S11. Manipulation.
Movie S12. Reachable workspace for a single triangle.
References (*54*–*59*)

REFERENCES AND NOTES

1. M. Yim, W.-M. Shen, B. Salemi, D. Rus, M. Moll, H. Lipson, E. Klavins, G. S. Chirikjian, Modular self-reconfigurable robot systems [grand challenges of robotics]. *IEEE Robot. Autom. Mag.* **14**, 43–52 (2007).
2. H. Ahmadzadeh, E. Masehian, M. Asadpour, Modular robotic systems: Characteristics and applications. *J. Intell. Robot. Syst.* **81**, 317–357 (2016).
3. J. W. Romanishin, K. Gilpin, D. Rus, M-blocks: Momentum-driven, magnetic modular robots, in *Proceedings of the 2013 IEEE/RSJ International Conference on Intelligent Robots and Systems* (IEEE, 2013), pp. 4288–4295.
4. G. Jing, T. Tosun, M. Yim, H. Kress-Gazit, An end-to-end system for accomplishing tasks with modular robots, in *Proceedings of Robotics: Science and Systems* (RSS Foundation, 2016), p. 25.
5. F. Nigl, S. Li, J. E. Blum, H. Lipson, Structure-reconfiguring robots: Autonomous truss reconfiguration and manipulation. *IEEE Robot. Autom. Mag.* **20**, 60–71 (2013).
6. S. K. Yun, D. A. Hjelle, E. Schweikardt, H. Lipson, D. Rus, Planning the reconfiguration of grounded truss structures with truss climbing robots that carry truss elements, in *Proceedings of the 2009 IEEE International Conference on Robotics and Automation* (IEEE, 2009), pp. 1327–1333.
7. B. Jenett, A. Abdel-Rahman, K. Cheung, N. Gershenfeld, Material–robot system for assembly of discrete cellular structures. *IEEE Robot. Autom. Lett.* **4**, 4019–4026 (2019).
8. K. H. Petersen, R. Nagpal, J. K. Werfel, Termes: An autonomous robotic system for three-dimensional collective construction, in *Robotics: Science and Systems VII*, H. Durrant-Whyte, N. Roy, P. Abbeel, Eds. (MIT Press, 2011).
9. G. J. Hamlin, A. C. Sanderson, Tetrobot: A modular approach to parallel robotics. *IEEE Robot. Autom. Mag.* **4**, 42–50 (1997).
10. R. Kovacs, A. Ion, P. Lopes, T. Oesterreich, J. Filter, P. Otto, T. Arndt, N. Ring, M. Witte, A. Synytsia, P. Baudisch, TrussFormer: 3D printing large kinetic structures, in *Proceedings of the 31st Annual ACM Symposium on User Interface Software and Technology* (ACM, 2018), pp. 113–125.
11. P. C. Hughes, W. G. Sincarsin, K. A. Carroll, Trussarm—A variable-geometry-truss manipulator. *J. Intell. Mater. Syst. Struct.* **2**, 148–160 (1991).
12. S. Curtis, M. Brandt, G. Bowers, G. Brown, C. Cheung, C. Cooperider, M. Desch, N. Desch, J. Dorband, K. Gregory, K. Lee, Tetrahedral robotics for space exploration, in *Proceedings of 2007 IEEE Aerospace Conference* (IEEE, 2007), pp. 1–9.
13. J. C. Zagal, C. Armstrong, S. Li, Deformable octahedron burrowing robot, in *Proceedings of Artificial Life Conference* (International Society of Artificial Life, 2012), pp. 431–438.
14. A. Spinos, D. Carroll, T. Kientz, M. Yim, Variable topology truss: Design and analysis, in *Proceedings of the 2017 IEEE/RSJ International Conference on Intelligent Robots and Systems* (IEEE, 2017), pp. 2717–2722.
15. A. Spinos, M. Yim, Towards a variable topology truss for shoring, in *Proceedings of the 2017 14th International Conference on Ubiquitous Robots and Ambient Intelligence* (IEEE, 2017), pp. 244–249.
16. A. Lyder, R. F. Garcia, K. Stoy, Mechanical design of odin, an extendable heterogeneous deformable modular robot, in *Proceedings of 2008 IEEE/RSJ International Conference on Intelligent Robots and Systems* (IEEE, 2008), pp. 883–888.
17. C. H. Yu, K. Haller, D. Ingber, R. Nagpal, Morpho: A self-deformable modular robot inspired by cellular structure, in *Proceedings of the 2008 IEEE/RSJ International Conference on Intelligent Robots and Systems* (IEEE, 2008), pp. 3571–3578.
18. S. Takei, M. Iida, T. Naemura, Kinereels: Extension actuators for dynamic 3D shape, in *ACM SIGGRAPH 2011 Posters* (ACM, 2011), p. 84.
19. S. Jeong, B. Kim, S. Park, E. Park, A. Spinos, D. Carroll, T. Tsabedze, Y. Weng, T. Seo, M. Yim, F. C. Park, Variable topology truss: Hardware overview, reconfiguration planning and locomotion, in *Proceedings of the 2018 15th International Conference on Ubiquitous Robots* (Korea Robotics Society, 2018), pp. 610–615.
20. Z. M. Hammond, N. S. Usevitch, E. W. Hawkes, S. Follmer, Pneumatic reel actuator: Design, modeling, and implementation, in *Proceedings of 2017 IEEE International Conference on Robotics and Automation* (IEEE, 2017), pp. 626–633.
21. N. S. Usevitch, A. M. Okamura, E. W. Hawkes, APAM: Antagonistic pneumatic artificial muscle, in *Proceedings of the 2018 IEEE International Conference on Robotics and Automation* (IEEE, 2018), pp. 1539–1546.
22. J. Friesen, A. Pogue, T. Bewley, M. de Oliveira, R. Skelton, V. Sunspiral, DuCTT: A tensegrity robot for exploring duct systems, in *Proceedings of the 2014 IEEE International Conference on Robotics and Automation* (IEEE, 2014), pp. 4222–4228.
23. A. P. Sabelhaus, J. Bruce, K. Caluwaerts, P. Manovi, R. F. Firoozi, S. Dobi, A. M. Agogino, V. SunSpiral, System design and locomotion of SUPERball, an untethered tensegrity robot, in *Proceedings of the 2015 IEEE International Conference on Robotics and Automation* (IEEE, 2015), pp. 2867–2873.
24. L. H. Chen, K. Kim, E. Tang, K. Li, R. House, E. L. Zhu, K. Fountain, A. M. Agogino, A. Agogino, V. Sunspiral, E. Jung, Soft spherical tensegrity robot design using rod-centered actuation and control. *J. Mech. Robot.* **2**, (2017).
25. J. Bruce, A. P. Sabelhaus, Y. Chen, D. Lu, K. Morse, S. Milam, K. Caluwaerts, A. M. Agogino, V. SunSpiral, SUPERball: Exploring tensegrities for planetary probes, in *Proceedings of 12th International Symposium on Artificial Intelligence, Robotics and Automation in Space* (i-SAIRAS, 2014).
26. C. Paul, J. W. Roberts, H. Lipson, F. V. Cuevas, Gait production in a tensegrity based robot, in *Proceedings of 2005 IEEE International Conference on Advanced Robotics* (IEEE, 2005), pp. 216–222.
27. S. Murata, D. Jodoi, H. Furuya, Y. Terada, K. Takadama, Inflatable tensegrity module for a large-scale space structure and its construction scenario, in *56th International Astronautical Congress of the International Astronautical Federation, the International Academy of Astronautics, and the International Institute of Space Law* (AIAA, 2005).
28. J. Dessi-Olive, J. Case, M. Koliner, V. T. Meda, Self-deploying tensegrity structures with inflatable struts, in *Proceedings of the International Association for Shell and Spatial Structures* (IASS, 2019), pp. 1–8.
29. D. Rus, M. T. Tolley, Design, fabrication and control of soft robots. *Nature* **521**, 467–475 (2015).
30. C. Majidi, Soft robotics: A perspective—Current trends and prospects for the future. *Soft Robot.* **1**, 5–11 (2014).
31. E. W. Hawkes, M. R. Cutkosky, Design of materials and mechanisms for responsive robots. *Annu. Rev. Control Robot. Auton. Syst.* **1**, 359–384 (2018).
32. S. I. Rich, R. J. Wood, C. Majidi, Untethered soft robotics. *Nat. Electron.* **2**, 102–112 (2018).
33. X. Huang, K. Kumar, M. K. Jawed, A. M. Nasab, Z. Ye, W. Shan, C. Majidi, Chasing biomimetic locomotion speeds: Creating untethered soft robots with shape memory alloy actuators. *Sci. Robot.* **3**, eaau7557 (2018).
34. M. T. Tolley, R. F. Shepherd, B. Mosadegh, K. C. Galloway, M. Wehner, M. Karpelson, R. J. Wood, G. M. Whitesides, A resilient, untethered soft robot. *Soft Robot.* **1**, 213–223 (2014).
35. R. Niiyama, D. Rus, S. Kim, Pouch motors: Printable/inflatable soft actuators for robotics, in *Proceedings of the 2014 IEEE International Conference on Robotics and Automation* (IEEE, 2014), pp. 6332–6337.
36. A. D. Marchese, C. D. Onal, D. Rus, Autonomous soft robotic fish capable of escape maneuvers using fluidic elastomer actuators. *Soft Robot.* **1**, 75–87 (2014).
37. M. Wehner, R. L. Truby, D. J. Fitzgerald, B. Mosadegh, G. M. Whitesides, J. A. Lewis, R. J. Wood, An integrated design and fabrication strategy for entirely soft, autonomous robots. *Nature* **536**, 451–455 (2016).
38. N. W. Bartlett, M. T. Tolley, J. T. Overvelde, J. C. Weaver, B. Mosadegh, K. Bertoldi, G. M. Whitesides, R. J. Wood, A 3D-printed, functionally graded soft robot powered by combustion. *Science* **349**, 161–165 (2015).
39. M. Loepfe, C. M. Schumacher, U. B. Lustenberger, W. J. Stark, An untethered, jumping roly-poly soft robot driven by combustion. *Soft Robot.* **2**, 33–41 (2015).
40. M. Wehner, M. T. Tolley, Y. Mengüç, Y. L. Park, A. Mozeika, Y. Ding, C. Onal, R. F. Shepherd, G. M. Whitesides, R. J. Wood, Pneumatic energy sources for autonomous and wearable soft robotics. *Soft Robot.* **1**, 263–274 (2014).
41. M. Takeichi, K. Suzumori, G. Endo, H. Nabae, Development of a 20-m-long Giacometti arm with balloon body based on kinematic model with air resistance, in *Proceedings of the 2017 IEEE/RSJ International Conference on Intelligent Robots and Systems* (IEEE, 2017), pp. 2710–2716.
42. S. Voisembert, A. Riwan, N. Mechbal, A. Barraco, A novel inflatable robot with constant and continuous volume, in *Proceedings of the 2011 IEEE International Conference on Robotics and Automation* (IEEE, 2011), pp. 5843–5848.
43. Y. A. Seong, R. Niiyama, Y. Kawahara, Low-pressure soft inflatable joint driven by inner tendon, in *2019 2nd IEEE International Conference on Soft Robotics* (IEEE, 2019), pp. 37–42.
44. A. Stilli, H. A. Wurdemann, K. Althoefer, A novel concept for safe, stiffness-controllable robot links. *Soft Robot.* **4**, 16–22 (2017).
45. H. Sareen, U. Umapathi, P. Shin, Y. Kakehi, J. Ou, H. Ishii, P. Maes, Printflatables: Printing human-scale, functional and dynamic inflatable objects, in *Proceedings of the 2017 CHI Conference on Human Factors in Computing Systems* (ACM, 2017), pp. 3669–3680.
46. S. Swaminathan, M. Rivera, R. Kang, Z. Luo, K. B. Ozutemiz, S. E. Hudson, Input, output and construction methods for custom fabrication of room-scale deployable pneumatic structures, in *Proceedings of the ACM on Interactive, Mobile, Wearable and Ubiquitous Technologies* (ACM, 2019).
47. W. B. Fichter, "A theory for inflated thin-wall cylindrical beams" (NASA Technical Note D-3466, NASA, 1966).
48. R. L. Comer, S. Levy, Deflections of an inflated circular-cylindrical cantilever beam. *AIAA J.* **1**, 1652–1655 (1963).
49. Y. He, W. Chen, Experiment and theoretical analysis study of ETFE inflatable tubes. *Int. J. Aerosp. Eng.* **2014**, 925428 (2014).
50. T. Yoshikawa, Manipulability of robotic mechanisms. *Int. J. Robot. Res.* **4**, 3–9 (1985).
51. S. A. Wainwright, W. D. Biggs, J. D. Currey, *Mechanical Design in Organisms* (Princeton Univ. Press, 1982).

52. S. Follmer, D. Leithinger, A. Owal, A. Hogge, H. Ishii, inFORM: Dynamic physical affordances and constraints through shape and object actuation, in *ACM Symposium on User Interface Software and Technology* (ACM, 2013), vol. 13, pp. 417–426.
53. N. S. Usevitch, Z. Hammond, S. Follmer, M. Schwager, Linear actuator robots: Differential kinematics, controllability, and algorithms for locomotion and shape morphing, in *Proceedings of the 2017 IEEE/RSJ International Conference on Intelligent Robots and Systems* (IEEE, 2017), pp. 5361–5367.
54. C. R. Nesler, T. A. Swift, E. J. Rouse, Initial design and experimental evaluation of a pneumatic interference actuator. *Soft Robot.* **5**, 138–148 (2018).
55. J. P. Fay, C. R. Steele, Bending and symmetric pinching of pressurized tubes. *Int. J. Solids Struct.* **37**, 6917–6931 (2000).
56. K. Wakana, H. Namari, M. Konyo, S. Tadokoro, Pneumatic flexible hollow shaft actuator with high speed and long stroke motion, in *Proceedings of the 2013 IEEE International Conference on Robotics and Automation* (IEEE, 2013), pp. 357–363.
57. B. A. Baydere, S. K. Talas, E. Samur, A novel highly-extensible 2-DOF pneumatic actuator for soft robotic applications. *Sensors Actuators A Phys.* **281**, 84–94 (2018).
58. R. L. Foote, The volume swept out by a moving planar region. *Math. Mag.* **79**, 289–297 (2006).
59. F. C. Campbell, Fatigue, in *Elements of Metallurgy and Engineering Alloys* (ASM International, 2008), chap. 14, pp. 243–246.

Funding: S.F., A.M.O., E.W.H., and Z.M.H. acknowledge support from the NSF under grant no. 1637446. M.S. and N.S.U. acknowledge support from DARPA YFA under grant no. D18AP00064. M.S., S.F., E.W.H., Z.M.H., and N.S.U. acknowledge support from the NSF under grant no. 1925030. E.W.H. acknowledges support under NSF grant no. 1925373. **Author contributions:** N.S.U. and Z.M.H. designed and built the robot, performed the testing, and wrote the manuscript. A.M.O. and M.S. provided direction and edited the manuscript. S.F. and E.W.H. defined the project and edited the manuscript. **Competing interests:** All authors are inventors on patent application 62/900156 submitted by the Board of Trustees of the Leland Stanford Junior University that covers a constant volume inflated truss robot. **Data and materials availability:** All data needed to evaluate the conclusions of the paper are available in the paper or the Supplementary Materials.

Submitted 9 August 2019
Resubmitted 5 December 2019
Accepted 18 February 2020
Published 18 March 2020
10.1126/scirobotics.aaz0492

Citation: N. S. Usevitch, Z. M. Hammond, M. Schwager, A. M. Okamura, E. W. Hawkes, S. Follmer, An untethered isoperimetric soft robot. *Sci. Robot.* **5**, eaaz0492 (2020).

An untethered isoperimetric soft robot

Nathan S. Usevitch, Zachary M. Hammond, Mac Schwager, Allison M. Okamura, Elliot W. Hawkes and Sean Follmer

Sci. Robotics **5**, eaaz0492.
DOI: 10.1126/scirobotics.aaz0492